Structural landscape of the host antiviral restriction factor SAMD9

Junwei Zou[1,2,#], Xiaodan Chen[2,3,#], Haiqiang Wu[2,3,#], Zuxing Liang[2,4,#], Kankan Yang[2], Yong Wang[3,*], Xinlong Yan[1,*], Jun Ma[2,*]

[1]College of Life Science and Bioengineering, Beijing University of Technology, Beijing 100124, China

[2]Institute of Infectious Diseases, Shenzhen Bay Laboratory, Shenzhen 518132, China

[3]College of Veterinary Medicine, Anhui Agricultural University, Hefei 230036, China

[4]College of Life Science, Capital Normal University, Beijing 100875, China

[#]These authors contributed equally: Junwei Zou, Xiaodan Chen, Haiqiang Wu, Zuxing Liang

*Correspondence: Jun Ma (majun@szbl.ac.cn); Xinlong Yan (yxlong2000@bjut.edu.cn); Yong Wang (wangyong119@ahau.edu.cn)

Abstract

Signal Transduction ATPases with Numerous Domains (STAND) proteins function as nucleotide-regulated molecular switches that undergo conformational transitions and higher-order assembly to govern innate immunity. Sterile alpha motif domain-containing 9 (SAMD9), an antiviral restriction factor within the STAND family linked to severe human inflammatory and hematological disorders, lacks a defined structural framework, and whether it follows canonical STAND activation principles remains unknown. Here, we present high-resolution cryo-electron microscopy structures of the human SAMD9 catalytic and regulatory core across multiple conformational and oligomeric states. These structures reveal that SAMD9 exists as a dynamic structural ensemble, comprising a compact autoinhibited monomer, C_2-symmetric dimers, asymmetric assemblies, and higher-order oligomers. The monomeric state is pre-loaded with ATP yet remains conformationally restrained by an extensive SIR2–NOD–TPR interaction network, demonstrating that nucleotide occupancy alone is insufficient for activation. Reciprocal NOD-mediated dimerization preserves this autoinhibited architecture, whereas alternative SIR2-mediated assembly modes drive distinct interprotomer interface remodeling and local domain rearrangements. Biochemical analyses demonstrate that although the OB domain contributes to nucleic-acid recognition, nucleic-acid binding alone is insufficient to relieve autoinhibition. Mapping disease-associated variants onto these structures unveils multiple regulatory layers susceptible to pathogenic perturbation. Together, our findings define SAMD9 as a conformationally and oligomerically plastic STAND immune regulator, providing a structural framework to understand its antiviral function and disease-associated pathogenesis.

Introduction

The Signal Transduction ATPases with Numerous Domains (STAND) family comprises evolutionarily conserved molecular machines that serve as central hubs of innate immune surveillance from bacteria to mammals[1-4]. Upon sensing danger or pathogen-derived signals, canonical STAND proteins, including Apaf-1[5,6], NAIP/NLRC4[7-9], plant NLRs such as ZAR1[10,11], and bacterial antiviral STANDs (Avs3 and Avs4)[12], undergo nucleotide-dependent conformational rearrangements that drive higher-order assembly to initiate inflammation, programmed cell death, or host defense. Within this family, sterile alpha motif domain-containing 9 (SAMD9) and its paralog SAMD9-like (SAMD9L)[13,14] function as broad-spectrum host restriction factors, with their most prominent roles defined in poxviruses restriction[15-20], where viral antagonists such as C7[16,20,21] and K1[21] have evolved to counteract SAMD9/SAMD9L-mediated immunity. Additional antiviral activities have been reported against several RNA viruses, including rotaviruses[22], HIV-1[23,24], and flaviviruses[25]. However, whether SAMD9 operates via these canonical STAND activation principles or relies on distinct structural mechanisms remains unknown.

The physiological importance of SAMD9/SAMD9L is underscored by severe human immune and hematological disorders caused by their dysregulation. Gain-of-function (GoF) mutations in *SAMD9* cause MIRAGE (myelodysplasia, infection, restriction of growth, adrenal hypoplasia, genital phenotypes, and enteropathy) syndrome[26,27], whereas activating mutations in *SAMD9L* underlie Ataxia-pancytopenia syndrome (APC)[28,29]. Persistent SAMD9/SAMD9L activation exerts strong selective pressure on hematopoietic cells, frequently driving adaptive clonal evolution via chromosome 7 loss (monosomy 7) and paradoxically predisposing patients to myelodysplastic syndrome (MDS)[29,30] and acute myeloid leukemia (AML)[31]. Elucidating SAMD9/SAMD9L regulation is therefore important for understanding both antiviral defense and disease pathogenesis.

SAMD9/SAMD9L possess a multi-domain architecture comprising an N-terminal sterile alpha motif (SAM) domain[32], an AlbA2 (Schlafen-like) effector, a Sir2-like (SIR2) domain[17,33], a central nucleotide-binding oligomerization domain (NOD)[13], a tandem tetratricopeptide repeats (TPR) domain, and a C-terminal oligonucleotide/oligosaccharide-binding (OB) domain[13,22]. The SIR2 and NOD domains are implicated in nucleotide-dependent conformational regulation[13], the TPR region contributes to oligomerization[13], and the OB domain participates in nucleic-acid sensing or ligand recognition[22]. Although the AlbA2 domain binds nucleic acids including dsDNA[33] and inhibits viral protein synthesis through selective host $tRNA^{Phe}$ cleavage[17], how these modular domains are

spatially organized and functionally coordinated to maintain latency and trigger activation remains unresolved. High-resolution structural characterization has long been challenging owing to massive molecular size (~190 kDa) and marked conformational heterogeneity of these proteins.

Here, we report the high-resolution cryo-electron microscopy (cryo-EM) structures of human SAMD9 spanning multiple conformational and assembly states. These structures define the molecular architecture of the SAMD9 catalytic and regulatory core and uncover how a multilayered network of intra- and interprotomer interactions governs its autoinhibition, oligomerization, and conformational plasticity. By integrating structural analysis with biochemical validation and disease-associated variant mapping, our work establishes a unified framework for SAMD9 regulation, expanding the structural paradigm of STAND-mediated innate immunity.

Results

SAMD9 exhibits conformational and oligomeric heterogeneity

Structural characterization of full-length human SAMD9 has been challenging due to its large size, intrinsic conformational flexibility, and limited biochemical stability. To overcome these limitations, we engineered a C-terminal core construct comprising residues 159–1589 (designated as SAMD9C) by removing the N-terminal SAM domain and its adjacent flexible linker (residues 1–158) (Figure 1A). This construct preserves the conserved catalytic and regulatory regions of SAMD9 while substantially improving recombinant expression and biochemical stability in a baculovirus–insect cell system. Purified SAMD9C exhibited favorable biochemical properties, eluting as a sharp and monodisperse peak on size-exclusion chromatography (SEC) (Figure S1).

An initial single-particle cryo-EM analysis yielded a 2.8 Å reconstruction of the SAMD9C monomer (Figure 1B and Figure S2; Table S1). Despite its apparent chromatographic homogeneity, however, 2D class averages revealed pronounced oligomeric heterogeneity, with particles ranging from monomers and putative C_2-symmetric dimers to higher-order oligomers, including trimers, tetramers, and extended assemblies built upon the C_2-dimeric core (Figure 1C). Severe preferred orientation in this dataset nevertheless precluded reliable 3D reconstruction of these additional states.

To mitigate this limitation, we supplemented SAMD9C with the detergent lauryl maltose neopentyl glycol (LMNG) during cryo-EM sample preparation. The resulting dataset enabled 3D classification of multiple conformational and oligomeric states, including a compact monomer (3.12

Å), which closely matched the monomer structure obtained from the initial dataset; two closely related C_2-symmetric dimers (state 1, 3.20 Å; state 2, 3.01 Å); a C_2-symmetric dimer associated with a substoichiometric third protomer (3.38 Å); two partial asymmetric dimers (state 1, 3.88 Å; state 2, 3.68 Å); and a substoichiometric asymmetric trimer (3.86 Å) (Figure S3).

Particle distributions further indicated that SAMD9C predominantly exists as monomers (~39%) and C_2-symmetric dimers (~45%), with the remaining particles distributed among asymmetric assemblies (~16%) (Figure S3). Together, these structures reveal that SAMD9C does not adopt a single defined oligomeric state but instead samples a heterogeneous ensemble of symmetric and asymmetric assemblies, establishing conformational and oligomeric plasticity as a defining feature of its molecular architecture.

The SAMD9C monomer adopts a compact autoinhibited conformation

The cryo-EM map of the monomeric SAMD9C establishes a compact core architecture comprising residues 386–1589, whereas the N-terminal AlbA2 domain (residues 159–385) was poorly resolved, indicating substantial conformational flexibility relative to the core (Figures 1A and 1B). The well-resolved region sequentially integrates the SIR2 (residues 386–623), NOD (residues 624–1001), TPR (residues 1002–1424), and OB (residues 1425–1589) domains into a compact SIR2–NTPase–TPR–OB module that adopts a characteristic G-shaped, "closed" conformation.

Structure-similarity searches using DALI[34] retrieved no significant structural homolog of the SAMD9C architecture, highlighting the distinctive global organization of its multidomain core. At the individual-domain level, however, SAMD9C modules show similarity to representative structures from distinct protein families (Figure S4A). The SIR2 domain adopts a canonical sirtuin-like Rossmann fold, exemplified by the yeast sirtuin Hst2[35]. The NOD domain exhibits a P-loop NTPase fold related to AAA+ ATPases such as TRIP13[36]. The TPR domain forms a curved solenoid scaffold resembling tetratricopeptide repeat proteins such as PEAK3[37]. The C-terminal OB domain adopts a canonical OB-fold architecture, consistent with RNA-binding OB domains represented by YB-1[38].

The compact closed conformation of SAMD9C is maintained by four interconnected interdomain interaction networks that collectively restrain its activation machinery and stabilize an autoinhibited state (Figure 1D). First, the C-terminal OB domain is positioned adjacent to the NOD module, forming a putative OB–NOD interface (Figure 1D, Panel 1). Although side-chain densities within this region are insufficient for definitive contact assignment, AlphaFold3 modeling predicts a

discrete network of polar interactions, including two potential salt bridges ($Lys726_{NOD}$–$Asp1516_{OB}$ and $Arg824_{NOD}$–$Glu1568_{OB}$) and a hydrogen bond ($Ile823_{NOD}$–$Ser1563_{OB}$). These contacts suggest that the OB domain contributes to conformational restraint, although its relatively dynamic or transient nature indicates an auxiliary role rather than the primary autoinhibitory latch. Second, the OB and TPR domains form an extensive interface stabilized by an integrated network of polar and hydrophobic contacts (Figure 1D, Panel 2). Electrostatic interactions and hydrogen bonds involving both side-chain and backbone atoms are contributed by TPR residues (Glu1171, Glu1174, Asp1190, Thr1191, Tyr1274, Val1276, Leu1277, Lys1279, and Arg1281) and OB residues (His1470, His1472, Arg1473, Thr1474, Lys1475, Gln1476, Ile1478, and Tyr1480), complemented by a cation–π interaction between $Lys1475_{OB}$ and $Tyr1274_{TPR}$. This network is further reinforced by hydrophobic packing between TPR residues (Tyr1192, Val1276, Leu1277, and Leu1278) and an OB hydrophobic patch (Phe1464, Tyr1468, Met1471, His1472, Tyr1480, and Ile1578). Third, the NOD and TPR domains engage through an additional interface centered on electrostatic interactions mediated by Arg1187 and Arg1188 of the TPR domain (Figure 1D, Panel 3). Arg1187 forms hydrogen bonds and salt bridges with Lys766, Asp769, and the Phe770 backbone within NOD, whereas Arg1188 anchors Asp805 and Asn806 of NOD, further constraining the local NOD–TPR arrangement. Finally, the SIR2 domain functions as a structural latch that reinforces the central SIR2–NOD–TPR junction (Figure 1D, Panel 4). $Glu411_{SIR2}$ contacts $Cys979_{NOD}$, while $Asp532_{SIR2}$ engages the $Gly1023_{NOD}$ backbone and the $Lys1024_{TPR}$ side chain. Together, these coordinated interaction networks form a distributed structural constraint system that locks SAMD9C into a compact inactive conformation, thereby preventing spontaneous activation prior to appropriate immune stimulation.

Together, the SIR2–NOD–TPR network and the spatial confinement of the OB domain define a compact architecture consistent with a restrained basal state. To test whether this compact architecture corresponds to a catalytically inactive conformation, we examined both ATPase and NADase activities of purified SAMD9C using complementary biochemical assays. SAMD9C exhibited negligible ATP hydrolysis and undetectable NAD^+ hydrolysis activity under all tested conditions, including the presence of diverse nucleic-acid substrates or nucleotide cofactors (Figures S4C and S4D). In parallel, the positive controls DdmD[39,40] and *E. coli* Avs5[41,42] displayed robust ATPase and NADase activities, respectively, validating the assay conditions. These biochemical results are consistent with the cryo-EM structure, in which the compact

SIR2–NOD–TPR–OB arrangement constrains the conformational rearrangements required for activation. Analogous to the autoinhibited states of other STAND-family proteins, including Apaf-1[5], NLRC4[7], and ZAR1[10], SAMD9C appears to rely on coordinated intramolecular constraints to maintain the NOD-containing activation machinery in a latent state prior to productive oligomerization. Thus, the compact monomeric structure suggests that SAMD9C autoinhibition arises from distributed multi-domain structural constraints rather than a single dominant interface.

SAMD9 is pre-loaded with ATP in the autoinhibited state

Within the high-resolution cryo-EM density of the SAMD9C monomer, we identified an ATP molecule and a coordinated Mg^{2+} ion bound within the conserved nucleotide-binding pocket of the NOD domain (Figure 1E). The ligand density was clearly resolved, enabling unambiguous modeling of the adenine, ribose, triphosphate moieties, and associated metal coordination. The adenine ring is accommodated within an aromatic pocket via π–π stacking with Phe683 and Phe865, complemented by hydrophobic contacts with Tyr684 and Phe705. The ribose moiety is anchored by backbone hydrogen bonds with Phe683, Tyr684, Gly686 and Gly687. Meanwhile, the triphosphate group is coordinated by the P-loop backbone (Gly740–Thr745) and a salt bridge with Arg837, with His737 further stabilizing the β/γ-phosphate oxygens through hydrogen bonding. Additionally, a Mg^{2+} ion adopts an octahedral coordination geometry with the β/γ-phosphate oxygens and the Thr744 side-chain hydroxyl group, stabilizing the ATP-bound configuration (Figure 1E).

Notably, ATP occupancy distinguishes SAMD9 from canonical STAND ATPases, such as Apaf-1[5], NLRC4[7], and NOD2[43], whose autoinhibited states are typically associated with ADP and require ADP-to-ATP exchange coupled to large-scale conformational rearrangements that promote oligomerization and activation. In contrast, the monomeric SAMD9C accommodates ATP while remaining in a compact, conformationally restrained architecture. This finding indicates a distinct regulatory paradigm in which nucleotide loading alone is insufficient to trigger conformational activation. Instead, SAMD9 adopts a "primed-but-inhibited" state in which the NOD domain is pre-loaded with ATP yet held in check by extensive interdomain interactions, indicating that nucleotide occupancy and conformational activation are mechanistically separable.

Structural basis of SAMD9 C_2-symmetric dimerization

3D classification of the SAMD9C cryo-EM dataset resolved a predominant C_2-symmetric dimer, accounting for approximately 74% of dimeric particles (Figure 2A and Figure S3; Table S1). This assembly is mediated by a reciprocal, head-to-head interface exclusively between central NOD domains, leaving the peripheral SIR2 and TPR–OB modules spatially separated (Figures 2A and 2B). The C_2-symmetric dimer interface is mediated by an extensive NOD–NOD' interaction network dominated by electrostatic and hydrogen-bonding contacts (Figure 2B, right). Key polar interactions involve Glu699, Ser700, and Glu874 from one protomer with Lys860', Arg863', Ala864', and Lys870' from the opposing protomer, establishing a symmetric association. In addition, a cation–π interaction between Arg863' and Tyr701, together with local Pro704–Pro704' packing, further reinforces the dimer interface. Further classification identified two closely related dimeric states differing primarily by a subtle rigid-body rotation of one protomer relative to the other—transitioning into a more expanded conformation—occurring without internal protomer remodeling (Cα RMSD = 0.7 Å) or interface disruption (Figure S4D).

Dimerization via this C_2 interface induces minimal conformational perturbation within individual protomers, which retain the compact autoinhibited architecture observed in the monomer (Cα RMSD = 1.1 Å) (Figure S4E). Thus, C_2-symmetric dimerization does not disrupt the closed protomer architecture, but rather establishes a dynamic, conformationally plastic oligomeric state that likely reflects the monomer–dimer equilibrium of SAMD9 in solution.

Substoichiometric engagement of a third protomer via SIR2–OB interactions

In addition to the predominant C_2-symmetric dimer, 3D classification with C_1 symmetry identified a substoichiometric assembly (~26% of dimeric particles) in which a third protomer—represented solely by its TPR–OB module (residues 1343–1589)—associates with the SIR2 domain of one protomer within the canonical C_2-symmetric dimer (Figure 2C and Figure S3; Table S1). Within this asymmetric complex, the underlying dimeric core closely resembles the more expanded C_2-symmetric dimer state (Cα RMSD = 0.3 Å; Figure S4F) described above, indicating that recruitment of the third protomer does not substantially perturb the canonical dimeric core.

Engagement of the third protomer is mediated exclusively through an intermolecular SIR2'–OB'' interface between its C-terminal OB domain and one core protomer (Figure 2D, left). This interface is stabilized by a composite network of polar, electrostatic, and hydrophobic interactions (Figure 2D, right). A tight polar network is established by backbone and side-chain

contacts involving SIR2' residues (Lys456, Arg497, Ala461, Asn462, Leu463, Asn484, and Tyr505) and OB'' residues (Glu1535, Arg1562, Ser1563, Gly1564, Arg1565, and Glu1568). In particular, this network is anchored by a prominent $Lys456_{SIR2'}$–$Glu1568_{OB''}$ salt bridge. Furthermore, $Ile1567_{OB''}$ inserts into a hydrophobic pocket formed by His464, Phe465, Val468, Ile500, and Tyr505 of SIR2', providing a key nonpolar anchor that reinforces the SIR2'–OB'' association.

Crucially, the TPR–OB module exhibits conformational versatility: it is positioned adjacent to the internal OB domain within a single protomer, but engages the SIR2′ domain of a neighboring subunit across protomers. Structural comparison confirms that these intramolecular and intermolecular modes are mutually sterically compatible (Figure S4G). Consequently, SAMD9C integrates the NOD–NOD dimeric interface with flexible SIR2–OB intermolecular contacts—enabled by the intrinsic positional plasticity of the TPR–OB region—to accommodate higher-order protomer recruitment without disrupting its primary autoinhibited architecture.

SIR2-mediated assembly drives alternative SAMD9 oligomeric states

Beyond the predominant C_2-symmetric dimer, 3D classification identified a series of low-abundance asymmetric assemblies (approximately 11.5% of the total particles), comprising two partially asymmetric dimeric states and a substoichiometric asymmetric trimeric assembly (Figures 3A–3C and Figure S3; Table S2). These assemblies display pronounced structural heterogeneity through distinct inter-subunit contact modes and domain organization, yet each retains one intact, compactly folded SAMD9C protomer (Figures 3A–3C and Figure S5).

In asymmetric dimer 1, a fully closed SAMD9C protomer recruits an isolated SIR2' domain (residues 389–623) through a pseudo-C_2-symmetric SIR2–SIR2' interface (Figures 3A and 3D; Figure S5B). In asymmetric dimer 2, the second protomer provides an intact SIR2' domain, a TPR'–OB' module (residues 1099–1589), and an unmodeled, partially resolved NOD' region. In this state, the TPR'–OB' module relocates adjacent to its internal SIR2' domain, reflecting substantial peripheral rearrangement relative to the compact monomer (Figures 3B and 3E; Figure S5C). Extending this organization, the asymmetric trimer integrates a fully intact protomer, a fragmented second protomer (comprising SIR2'–NOD'–TPR' [residues 389–1094] and TPR'–OB' modules [residues 1327–1589]), and a third TPR''–OB'' (residues 1327–1589). Assembly is mediated by a pseudo-C_2 SIR2–SIR2' pairing and two distinct SIR2–OB contacts: TPR'–OB' interacts with the SIR2 (SIR2–OB interaction I), whereas TPR''–OB'' engages the SIR2' (SIR2–OB interaction II)

(Figures 3C and 3F; Figure S5D). Notably, the specific SIR2 partner engaged by the TPR–OB module differs between the asymmetric dimer 2 and the asymmetric trimer, underscoring the plasticity of these contacts (Figures 3E and 3F).

Despite their compositional differences, these asymmetric assemblies share a unifying organizing principle: protomer recruitment is primarily driven by a pseudo-C_2-symmetric SIR2–SIR2' interface rather than the NOD–NOD interaction (Figure 3G). This SIR2–SIR2' interface is centered around a reciprocal network of polar and electrostatic interactions (Figure 3G, right). Multiple symmetric hydrogen-bonding and electrostatic contacts involving Arg515, Gln514, Arg522, Gln565, Arg553, Arg593, Tyr564, and Leu594 from opposing protomers establish a tightly interconnected interprotomer interface that stabilizes the SIR2–SIR2' association. Importantly, SIR2–SIR2' pairing is sterically incompatible with the compact, closed conformation. Engagement of SIR2' domain introduces severe steric clashes between the TPR–OB modules of two closed protomers (Figure S6A). Accommodating SIR2–SIR2' pairing thus necessitates the physical displacement of relevant TPR'–OB' regions, driving partial subunit opening and domain remodeling.

Crucially, structural comparison across all four identified SIR2–OB interfaces—including those in the C_2 dimer-associated trimer, asymmetric dimer 2, and the asymmetric trimer—reveals virtually identical interaction geometries (Figure S6B). This conservation identifies the SIR2–OB contact as a major interaction node. Large-scale physical displacement of the TPR–OB module, followed by its re-engagement with SIR2, represents a key mechanism stabilizing intermolecular association across diverse SAMD9C oligomeric states.

Together, these structures demonstrate that SAMD9 populates a dynamic assembly landscape characterized by alternative interprotomer interfaces and accompanying domain rearrangements. Whereas NOD–NOD pairing preserves the compact autoinhibited dimer, SIR2-mediated assembly drives higher-order, conformationally plastic oligomers coupled to TPR–OB displacement, providing a structural basis for the SAMD9 conformational diversity.

The OB domain is insufficient to release SAMD9 autoinhibition

To investigate whether the C-terminal OB domain contributes to SAMD9C autoinhibition, we characterized a truncated SAMD9C variant lacking the OB domain (SAMD9C$^{\Delta OB}$; residues 159–1426). Single-particle cryo-EM analysis of SAMD9C$^{\Delta OB}$ yielded high-resolution reconstructions of monomeric (2.93 Å; ~35% of particles), C_2-symmetric dimeric (2.74 Å; ~40% of particles), and

asymmetric dimeric states (2.74 Å; ~25% of particles) (Figure 4 and Figure S7; Table S3). These assembly states closely recapitulate the canonical monomer, C_2 dimer, and asymmetric dimer 1 of wild-type SAMD9C in both structural architecture (Cα RMSD ≈ 0.9 Å) and relative particle populations, aside from the expected truncation of the OB domain and flexible C-terminal TPR elements (Figures S8A and S8B). Across all three states, intact protomers are consistently resolved for residues 386–1307; within the asymmetric dimer, one protomer additionally recruits an isolated SIR2 domain (residues 387–621), demonstrating that OB domain removal leaves the SIR2–SIR2'-mediated association intact (Figure 4B). However, owing to the deletion of the OB domain, higher-order configurations corresponding to wild-type asymmetric dimer 2 and the asymmetric trimer were absent.

Notably, beyond the missing TPR–OB module, the autoinhibitory SIR2–NOD–TPR interface remains fully intact and structurally indistinguishable from wild-type protein. Consistent with the structural observation that the compact SAMD9C architecture lacks an extensive, direct OB–NOD contact, *in vitro* biochemical assays confirmed that SAMD9C$^{\Delta OB}$ remains enzymatically latent, displaying no detectable ATPase or NADase activity (Figures S9C and S9D). Together, these structural and functional findings demonstrate that OB domain removal alone is insufficient to drive conformational opening or unleash enzymatic activity. Instead, full release of autoinhibition requires coordinated disruption of the extensive SIR2–NOD–TPR core to trigger productive activation.

SAMD9 employs distinct domain contributions for broad nucleic acid recognition

Given that SAMD9 harbors an N-terminal AlbA2 domain associated with nuclease activity[17,33]and a C-terminal OB domain characteristic of single-stranded nucleic acid-binding proteins[22], we sought to define how these modules coordinate nucleic acid recognition and whether substrate engagement is coupled to conformational activation. We generated a panel of truncation variants derived from SAMD9C, including an AlbA2-deletion (SAMD9C$^{\Delta AlbA2}$), an OB-deletion (SAMD9C$^{\Delta OB}$), a double-deletion (SAMD9C$^{\Delta AlbA2/\Delta OB}$), and the isolated AlbA2 domain, and evaluated their binding against diverse nucleic acid substrates (dsDNA, ssDNA, dsRNA, ssRNA, and tRNA^{Phe}) using electrophoretic mobility shift assays (EMSAs) (Figure 5).

Wild-type SAMD9C displayed broad and robust binding activity toward all tested substrates (Figure 5). Dissecting individual domain contributions revealed a clear functional partition among these modules. While simultaneous removal of both the AlbA2 and OB domains (SAMD9C$^{\Delta AlbA2/\Delta OB}$),

completely abolished detectable nucleic acid interaction, the isolated AlbA2 domain retained intrinsic binding activity across diverse nucleic acid species, consistent with its role as a broad-spectrum processing effector module[17,33]. In contrast, the OB-containing construct lacking AlbA2 (SAMD9C$^{\Delta AlbA2}$) displayed selective recognition of single-stranded species (ssDNA and ssRNA) and structured RNAs such as tRNA^{Phe}, demonstrating that the OB domain functions as a single-strand-substrate-selective sensor aligned with the canonical properties of OB folds. Notably, constructs retaining the central SIR2–NOD–TPR core (wild-type SAMD9C and SAMD9C$^{\Delta OB}$) exhibited substantially enhanced nucleic acid binding compared to the isolated AlbA2 domain alone, indicating that the central core serves as an essential architectural scaffold to promote efficient substrate capture. Together, these findings demonstrate that SAMD9C operates via a modular nucleic acid-recognition platform, in which the OB sensor confers structure-selective engagement, the AlbA2 effector provides broad-spectrum binding, and the central core optimizes substrate capture.

To establish the structural basis of OB-mediated single-stranded nucleic acid recognition, we compared the SAMD9 OB domain with established OB-fold proteins. The SAMD9 OB domain adopts a fold highly similar to the cold shock domain of human YB-1 (YB-1^{CSD}; PDB: 5YTX; RMSD = 4.7 Å)[38] (Figure S8E). Guided by this structural similarity, we generated an AlphaFold-based model of the SAMD9 OB domain bound to ssRNA (Figure S8F). In this model, ssRNA docks into a positively charged surface groove via electrostatic complementarity, engaging a basic residue cluster (Lys1454, Lys1461, Lys1465, Lys1469, Lys1473, and Arg1565) (Figure S8F, left). Superimposing this modeled OB–ssRNA complex into the autoinhibited SAMD9C$^{\Delta OB}$ cryo-EM structure revealed that nucleic acid binding is fully compatible with the compact architecture, causing no apparent steric clashes with either the potential intramolecular OB–NOD interface of the closed monomer or the intermolecular OB–SIR2 contact in asymmetric assemblies (Figure S8G and S8H).

These findings demonstrate that autoinhibition does not operate by sterically occluding the primary binding surface of the OB sensor. Furthermore, the capacity of the OB domain to engage nucleic acids without inducing global structural rearrangements indicates that substrate recognition by the sensor module alone is insufficient to trigger SAMD9 activation. Consistently, neither removal of the OB domain nor addition of nucleic acid substrates to wild-type SAMD9C was sufficient to induce detectable ATPase or NADase activity (Figures S9C and S9D), indicating that

substrate recognition alone is insufficient to trigger the conformational remodeling required for enzymatic activation.

Together, these results reveal a modular architecture in which SAMD9 decouples substrate recognition from catalytic activation: the C-terminal OB domain serves as a specialized sensor module to recognize specific single-stranded nucleic acid danger signals, whereas the N-terminal AlbA2 domain acts as a versatile effector domain providing baseline binding and nuclease capability. Crucially, the structural compatibility between substrate engagement and the autoinhibited state allows SAMD9 to maintain baseline nucleic acid surveillance without triggering premature, ectopic activation.

Higher-order SAMD9 assemblies suggest a link between oligomerization and conformational restraint

Cryo-EM analysis revealed that, beyond the predominant monomeric and dimeric species, SAMD9C populates a minor fraction of higher-order assemblies, including trimeric, tetrameric, and extended supramolecular structures (Figure 1C). Although the limited number of particles and severe preferred orientation precluded reliable 3D reconstruction of these assemblies, their overall organization was readily discerned through iterative 2D classification. Notably, these assemblies appear to be organized around the C_2-symmetric dimer: tetramers adopt a dimer-of-dimers configuration, extended filaments represent linear extensions of this repeating geometry, and trimers correspond to partial assemblies lacking one subunit or a C_2 dimer bound to an auxiliary protomer (Figure 1C). A composite model of the extended assembly—generated by docking experimental C_2 dimers into the 2D class envelope—yielded back-projections that closely recapitulated the experimental class averages, supporting a proposed sequential dimer-association mechanism (Figures 6A and 6B).

Inspection of this composite model revealed that inter-dimer assembly is primarily driven by reciprocal TPR–TPR contacts (residues 1320–1424) (Figure 6C). Crucially, the interacting TPR segments correspond precisely to the dynamic TPR–OB modules that undergo substantial spatial displacement and engage in intermolecular pairing in the asymmetric assemblies described above (Figure 6C). By engaging in recurrent TPR–TPR interactions across adjacent dimers, the highly dynamic TPR–OB module is effectively tethered and locked into place, forming the structural backbone of the elongated, filament-like assemblies.

This TPR–TPR-mediated immobilisation directly impacts the conformational landscape of SAMD9. Intermolecular engagement of the TPR segments restricts the rigid-body mobility of the structurally dynamic TPR–OB module, thereby imposing steric and energetic barriers that prevent its displacement—a prerequisite for transitioning from the compact closed state toward an activated, open conformation. Higher-order oligomerization may therefore act as a "conformational clamp", stabilizing the autoinhibited architecture through cooperative dimer–dimer packing.

Together, these observations demonstrate that SAMD9C can form higher-order filament-like assemblies via TPR–TPR-mediated association of C_2-symmetric dimers. By specifically sequestering and constraining the dynamic TPR–OB module, higher-order assembly does not merely expand the quaternary state of SAMD9, but functions as a conformational restraint mechanism to reinforce autoinhibition.

Structural insights into pathogenic SAMD9/SAMD9L variants

Germline mutations in SAMD9 and SAMD9L cause loss-of-function (LoF), gain-of-function (GoF), and dominant-negative effects underlying diverse multisystem clinical syndromes[26-31,44]. To explore the structural basis of these disease-associated variants, we mapped reported pathogenic substitutions onto the SAMD9C structures and an AlphaFold predicted SAMD9L model (Figure 7A). SAMD9 and SAMD9L exhibit high structural and sequence conservation (Cα RMSD = 0.9 Å across SAMD9C equivalent regions; 61% full-length sequence identity) (Figure S9), supporting SAMD9C as a reliable structural surrogate for SAMD9L variant. To date, 95 variants have been associated with SAMD9-related disorders and 67 with SAMD9L-related phenotypes (Figure S10)[44,45].

Excluding variants located within the unresolved N-terminal region (residues 1–358; 8 in SAMD9 and 3 in SAMD9L), cannot be unambiguously interpreted within the current structural framework variants (11 variants in SAMD9 and 5 in SAMD9L), nonsense/frameshift mutations resulting in truncated products (3 variants for SAMD9 and 7 for SAMD9L), and buried substitutions primarily affect core domain stability (42 in SAMD9, 31 in SAMD9L) (Figure S10), the remaining structurally interpretable variants fall into four structural categories according to the regulatory elements they potentially perturb (Figure 7A and Figure S10). (1) Perturbation of NOD conformational dynamics and nucleotide binding: Substitutions at the inter-lobe interface of the NOD domain (R685Q, E712K, T767I/K, R982C/H in SAMD9; G690D, K770E, F869S, M892R, D934H, I972T, R986C/H in SAMD9L) likely impair the inter-lobe flexibility required for nucleotide

coordination and activation-coupled conformational transitions. (2) Disruption of nucleic-acid sensing: Variants R1533Q (SAMD9) and R1460G (SAMD9L) map on the electropositive surface groove of the OB domain, predicted to compromise nucleic acid engagement. (3) Destabilization of autoinhibitory intraprotomer interfaces: A substantial cluster of variants maps to intramolecular contact sites that maintain the compact inactive state, including the SIR2–TPR interfaces (K643E, D769G/N, K1024E in SAMD9; R1028G in SAMD9L), the NOD–TPR interfaces (E803Q, E974K, R1188Q/P, D1190E/N in SAMD9), SIR2–NOD interface (R459C/S, N484S, and Y486S in SAMD9; S626L in SAMD9L), OB–NOD interface (R824Q, S1514N, and G1564S in SAMD9; R828Q in SAMD9L), and OB–TPR interface (Y1274C, V1276I, Q1286R, R1293Q/W, and I1478M in SAMD9; K1279E, R1281K/S, S1473N, and K1532N in SAMD9L). Perturbation of these coordinated domain interfaces shifts the conformational equilibrium toward a permissive, activated state. (4) Impairment of asymmetric interprotomer assembly: Variants F465L, I1567M, and K1569N in SAMD9 localize to the recurrent SIR2–OB interface, suggesting they alter the formation or stability in asymmetric state.

While these assignments provide a structural rationale for a substantial subset of pathogenic variants, functional validation in cellular and physiological contexts remains essential to establish how individual substitutions alter conformational dynamics, enzymatic activity, and antiviral immunity. Nevertheless, mapping disease variants across the SAMD9/SAMD9L structures establishes a unified structural model, illustrating how genetically diverse substitutions target distinct conformational checkpoints to yield broad molecular and clinical phenotypes.

Discussion

Here, we establish a structural framework defining SAMD9 as an allosterically flexible, multilayered immune regulator. Cryo-EM structures demonstrate that SAMD9 samples an ensemble of discrete architectural states, including a compact autoinhibited monomer, C_2-symmetric dimers, asymmetric assemblies, and higher-order oligomers. Rather than functioning as a binary switch, SAMD9 relies on coordinated intra- and interprotomer interfaces to shape its conformational landscape, coupleing autoinhibition, oligomerization, and functional plasticity.

The compact SAMD9C monomer represents the basal autoinhibited state, wherein extensive intraprotomer contacts constrain the SIR2, NOD, TPR, and OB domains into a closed, sterically sequestered architecture. Although ATP is bound within the NOD domain, this nucleotide-loaded state remains conformationally restrained, demonstrating that nucleotide occupancy alone is

insufficient for activation and must be integrated with allosteric interface remodeling. Whether nucleotide exchange or hydrolysis directly contributes to transitions among these conformational states remains to be determined.

Beyond the monomer, SAMD9 forms a predominant C_2-symmetric dimer via a reciprocal NOD–NOD interface while preserving the closed architecture of individual protomers. The subtle domain shifts between the two captured C_2-symmetric dimeric states highlight the intrinsic structural plasticity of this oligomeric scaffold. Sequential association of these dimers further generates tetramers and filament-like assemblies. Because this NOD-mediated oligomerization occurs without disrupting autoinhibition, these higher-order assemblies may serve as conformational reservoirs that maintain SAMD9 in a restrained state rather than representing terminal signaling complexes.

Beyond symmetric assemblies, our structures capture an alternative, asymmetric assembly mode mediated by recurrent SIR2–SIR2 and SIR2–OB interactions, accompanied by substantial repositioning of the TPR–OB module. These assemblies demonstrate that SAMD9 can access multiple oligomeric trajectories rather than following a single obligatory pathway. In this context, the SIR2–OB interaction likely functions as a flexible pivot, accommodating local movements of the TPR–OB module. Consistent with functional reports that the OB-fold domain is essential for SAMD9 oligomerization[22], these asymmetric assemblies are more consistent with functional intermediates connecting autoinhibited and activation-competent conformations.

These findings expand the mechanistic diversity of the STAND ATPase superfamily. Canonical STAND proteins—including Apaf-1[5,6], NAIP/NLRC4[7-9], NLRP3[46-48], plant NLRs (ZAR1[10,11]), and bacterial antiviral STANDs (Avs3/Avs4)[12]—undergo ligand-triggered, nucleotide-dependent conformational transitions that drive assembly into higher-order ring- or wheel-like architectures (e.g., apoptosomes, inflammasomes, and resistosomes). In contrast, SAMD9 bypasses large-scale single-step domain opening, instead operating like an allosteric rheostat. This mechanism resembles the stepwise activation trajectories observed in NAIP–NLRC4, while introducing a distinct mode of regulatory plasticity.

Together, these observations support a model in which SAMD9 homeostasis is maintained through a dynamic equilibrium between restrained oligomeric states and activation-competent conformations (Figure 7B). In the resting state, SAMD9 adopts a compact autoinhibited monomer that further self-associates through NOD–NOD interactions into C_2-symmetric dimers and higher-order assemblies, potentially providing a preorganized reservoir for rapid immune

responsiveness. Upon pathogen-associated molecular patterns (PAMPs) recognition, such as viral nucleic acids engagement by the OB domain, substrate binding may bias this equilibrium toward asymmetric remodeling involving SIR2–SIR2 and SIR2–OB interactions. These rearrangements could partially relieve autoinhibitory constraints within individual protomers, generating intermediate states that precede full catalytic activation. Whether SAMD9 ultimately forms higher-order ring-like effector assemblies analogous to inflammasomes or plant resistosomes remains an important question for future investigation[22].

This dynamic conformational framework provides a basis for understanding pathogenic *SAMD9* and *SAMD9L* variants. Disease-associated mutations map to multiple regulatory layers, including catalytic regions, nucleic acid-binding surfaces, autoinhibitory interfaces and oligomerization contacts. By destabilizing inhibitory constraints or shifting the oligomeric equilibrium, these variants may alter the threshold, magnitude, or duration of SAMD9-mediated immune responses, thereby contributing to human disease.

Several key questions remain unresolved. Defining how the N-terminal SAM domain integrates with C-terminal oligomerization will clarify whether SAM-mediated homotypic or heterotypic interactions regulate full-length assembly[32,49-51]. In addition, the physiological triggers and temporal sequence underlying these conformational transitions remain unclear. Although the OB domain provides selective recognition of single-stranded nucleic acids, whether substrate engagement functions as an allosteric cue in vivo requires further investigation. Finally, determining whether the extended filament-like assemblies observed here form in primary cells and contribute to antiviral defense will be essential for establishing their physiological relevance.

In summary, SAMD9 emerges as a highly plastic immune regulator controlled by a network of structural checkpoints rather than a simple on–off switch. By placing disease-associated mutations within this dynamic conformational framework, our study expands the structural paradigm of STAND-mediated signaling and provides a foundation for understanding and therapeutically targeting SAMD9/SAMD9L-associated disorders.

Materials and Methods

Protein expression and purification

The gene encoding full-length human SAMD9 (UniProt: Q5K651) was codon-optimized, synthesized, and cloned into the pFastBac-1 vector (Thermo Fisher Scientific) with a C-terminal Strep-tag for affinity purification. Truncated variants—including the structural core (SAMD9C, residues 159–1589) and versions lacking the AlbA2 domain (SAMD9C$^{\Delta AlbA2}$, residues 386–1589), the OB domain (SAMD9C$^{\Delta OB}$, residues 159–1426), or both (SAMD9C$^{\Delta AlbA2/\Delta OB}$, residues 386–1426)—were generated and purified using the same protocol. For biochemical studies, the isolated AlbA2 (residues 159–385) domain was subcloned into pET22b (Novagen) containing an N-terminal 6×His tag. All constructs and site-directed mutants were verified by DNA sequencing.

Eukaryotic SAMD9 constructs were expressed in *Spodoptera frugiperda* (Sf9) cells using the Bac-to-Bac expression system (Invitrogen). Cells were infected with recombinant baculovirus at a density of 2 × 10^6 cells/mL and harvested 72 h post-infection. Cell pellets were collected by centrifugation (1500 × *g*, 10 min) and resuspended in Lysis Buffer (50 mM Tris-HCl, pH 8.0, 500 mM NaCl, 5% glycerol) supplemented with cOmplete EDTA-free Protease Inhibitor Cocktail (Roche). Following sonication on ice, the lysate was clarified by centrifugation (20,000 × *g*, 1 h, 4°C). The supernatant was incubated with Strep-Tactin resin (IBA Lifesciences) for 1 h at 4°C, washed extensively with Lysis Buffer, and eluted with Lysis Buffer containing 50 mM D-biotin. The eluate was concentrated and further purified by size-exclusion chromatography (SEC) using a Superdex 200 Increase 10/300 GL column (Cytiva) in SEC buffer (50 mM Tris-HCl, pH 8.0, 150 mM NaCl). Fractions corresponding to a sharp, monodisperse peak were analyzed by SDS-PAGE, pooled, concentrated (Amicon Ultra, 50 kDa molecular mass cut-off (MWCO), Millipore). Samples were either used immediately for cryo-EM grid preparation or flash-frozen and stored at −80°C for subsequent biochemical assays.

The isolated AlbA2 was overexpressed in *Escherichia coli* BL21 (DE3) cells. Cultures were induced with 0.3 mM isopropyl-β-D-1-thiogalactopyranoside (IPTG) at OD600 ≈ 0.6 and grown at 16°C for 16–20 h. Cells were resuspended in Lysis buffer and disrupted using a high-pressure homogenizer. The His-tagged proteins were purified from the clarified supernatant using Ni-NTA Sepharose (GE Healthcare), washed with Lysis buffer containing 60 mM imidazole, and eluted with 300 mM imidazole. Target proteins were concentrated (10 kDa MWCO) and further purified by SEC using a Superdex 75 Increase 10/300 GL column. Fractions containing the target proteins were

pooled, concentrated, and flash-frozen for storage at −80°C for subsequent biochemical assays. At each purification step, protein purity and concentration were assessed by SDS-PAGE and NanoDrop (Thermo Fisher Scientific), respectively.

Cryo-EM Grid Preparation and Data Acquisition

Cryo-EM grids were prepared using a Vitrobot Mark IV (Thermo Fisher Scientific) maintained at 16°C and 100% humidity. For the SAMD9C and the SAMD9C$^{\Delta OB}$ variant, freshly purified protein samples were used directly for grid preparation. To improve particle distribution and mitigate preferred orientation of SAMD9C, LMNG was added to the SAMD9C sample to a final concentration of 0.001% (w/v) prior to grid preparation. For each sample, a 3-μL aliquot at a final concentration of 1.2 mg mL^{-1}, was applied to a freshly glow-discharged Quantifoil R2/1 300-mesh gold grid (Quantifoil Micro Tools GmbH). Following 10 s of incubation, the grids were blotted and vitrified by plunge-freezing into liquid ethane.

Cryo-EM data were acquired on a 300 kV Titan Krios microscope (Thermo Fisher Scientific) using a defocus range of -0.8 to -2.5 μm and a total dose of ~50 e^{-} Å^{-2} per movie. For the native SAMD9C and SAMD9C$^{\Delta OB}$ datasets, movies were recorded using EPU software on a Falcon 4 direct electron detector in super-resolution mode at a nominal magnification of ×165,000 (calibrated physical pixel size of 0.73 Å, 2.5 s exposure), yielding 2,602 and 5,576 micrographs, respectively. For the SAMD9C–LMNG dataset, data were collected using SerialEM[52] on a Gatan K3 direct electron detector with a BioQuantum GIF energy filter in counting mode at a nominal magnification of ×105,000 (calibrated physical pixel size of 0.83 Å), yielding 7,847 micrographs.

Image processing and 3D reconstruction

All cryo-EM data were processed using a consensus pipeline within cryoSPARC v5[53]. Movie stacks were subjected to beam-induced motion correction and contrast transfer function (CTF) estimation using Patch Motion Correction and Patch CTF Estimation, respectively. A consistent workflow was employed across all three datasets, integrating automated particle picking, multiple rounds of reference-free 2D classification to remove contaminants and poorly resolved particles, iterative 3D classification, and refinement. Global resolutions were determined using the gold-standard Fourier shell correlation (FSC) 0.143 criterion, with local resolutions estimated via the cryoSPARC implementation. Comprehensive processing workflows and reconstruction statistics are

detailed in Supplementary Figures S2, S3 and S7 and summarized in Supplementary Tables S1–S3.

For the initial SAMD9C dataset, 1,035,842 particles were initially identified by blob picking, and an additional 2,552,207 particles were identified by template-based picking from 2,602 micrographs. Following two rounds of 2D classification and removal of duplicate particles, 703,605 particles were retained for subsequent 3D analysis. Heterogeneous refinement and non-uniform refinement yielded a compact SAMD9C monomer at 2.80 Å resolution from 210,379 particles.

For the SAMD9C–LMNG dataset, 2,028,974 particles were initially picked from 7,847 micrographs using Topaz[54]. Following two rounds of 2D classification, 1,069,861 particles were retained for ab initio reconstruction and heterogeneous refinement. Subsequent 3D classification and non-uniform refinement resolved seven distinct conformational and oligomeric states: a monomer (3.12 Å, 297,392 particles), two C_2-symmetric dimers, designated C_2-asymmetric dimer 1 (3.20 Å, 123,958 particles) and C_2-asymmetric dimer 2 (3.01 Å, 225,983 particles), a C_2+1 trimer (3.38 Å, 124,016 particles), asymmetric dimer 1 (3.86 Å, 35,312 particles), asymmetric dimer 2 (3.68 Å, 24,252 particles), and an asymmetric trimer (3.88 Å, 26,959 particles). The addition of LMNG substantially improved particle angular distribution and facilitated structural characterization of multiple conformational and oligomeric states.

For the SAMD9C$^{\Delta OB}$ variant, 1,797,941 particles were initially picked by blob picking and 1,164,513 particles by Topaz picking from 5,576 micrographs. Following two rounds of 2D classification and removal of duplicate particles, 681,053 particles were retained for subsequent 3D analysis. Subsequent 3D classification and non-uniform refinement resolved three distinct states: a monomer, an asymmetric dimer, and a C_2-symmetric dimer, yielding final maps at 2.93 Å (161,221 particles), 2.90 Å (115,550 particles), and 2.74 Å (183,840 particles), respectively.

Model building and refinement

Model building was initiated using the high-resolution cryo-EM density map of the monomeric SAMD9C. An initial atomic model was generated by segmenting the AlphaFold 3-predicted[55] SAMD9 model into individual domains and docking them into the density map as rigid bodies using UCSF ChimeraX[56]. For the C_2-symmetric states of SAMD9C and the monomeric and dimeric states of SAMD9C$^{\Delta OB}$, initial models were generated by docking the refined SAMD9C monomer into the corresponding density maps. For the asymmetric assemblies from the SAMD9C–LMNG dataset,

initial models were generated by hybrid docking a relatively complete protomer together with individual domains into the corresponding densities, followed by extensive manual modification to account for conformational rearrangements at the interprotomer interfaces. All initial models were further improved through iterative cycles of manual adjustment in Coot[57] and real-space refinement in PHENIX[58]. Refinement was continued until model parameters converged and validation criteria, including MolProbity score, rotamer statistics, and Ramachandran statistics[59], met standard thresholds .

In the final atomic models, the AlbA2 domain (residues 159–385) was not resolved in any of the reconstructed states and was therefore excluded from all atomic models. Sequence coverage varied among the reconstructed assembly states. The SAMD9C monomer and C_2-symmetric dimer models comprise residues 386–1589. The C_2+1 trimer comprises two protomers spanning residues 386–1589 and a third protomer represented by a partial TPR–OB module (residues 1343–1589). Asymmetric dimers 1 and 2 each contain one protomer spanning residues 389–1589. The second protomer of asymmetric dimer 1 is represented by an isolated SIR2 domain (residues 389–623), whereas that of asymmetric dimer 2 comprises an SIR2 domain (residues 389–623) and a partial TPR–OB module (residues 1099–1589), respectively. The asymmetric trimer comprises one protomer spanning residues 389–1589, a second protomer comprising an SIR2–NOD–TPR region (residues 389–1094) and a partial TPR–OB module (residues 1327–1589), and a third protomer represented by a partial TPR–OB module (residues 1327–1589). Several flexible loops and linkers were excluded from the models because of insufficient density.

For the SAMD9C$^{\Delta OB}$ structures, both the monomer and the protomers of the C_2-symmetric dimer span residues 386–1307. The asymmetric dimer consists of one 386–1307 protomer and a partially resolved SIR2 segment (residues 387–621) from the second protomer. Unresolved regions within the TPR domain were excluded from the atomic models. The absence of the OB domain is consistent with the designed truncation.

Final model statistics and refinement parameters are summarized in Supplementary Tables S1–S3. Model building, structural analysis, and figure preparation were performed using UCSF ChimeraX, Coot, and PyMOL (https://pymol.org/).

Electrophoretic mobility shift assay (EMSA)

The nucleic acid-binding activity of human SAMD9C, its various truncated variants, and the isolated

AlbA2 domain toward diverse nucleic acid substrates (dsDNA, ssDNA, dsRNA, ssRNA, and tRNA) was evaluated by electrophoretic mobility shift assay (EMSA). Purified SAMD9C constructs at the indicated concentrations (ranging from 40 to 5,120 nM; representing protein-to-nucleic acid molar ratios from 1:1 to 128:1) were incubated with 40 nM 5'-FAM-labeled nucleic acid substrates in a 20 μl reaction volume containing EMSA buffer (20 mM Tris-HCl, pH 8.0, 100 mM NaCl). Following incubation for 30 min at room temperature, samples were mixed with 6× native gel loading buffer (non-denaturing) and resolved by 10% non-denaturing PAGE in 0.5× TG buffer (25 mM Tris-HCl, 192 mM glycine, pH 8.5) at 4°C. Gels were imaged using a Typhoon 5 Biomolecular Imager (Cytiva) according to the manufacturer's instructions.

All 5'-FAM-labeled oligonucleotides and complementary unlabeled strands were commercially synthesized and HPLC-purified. Substrates were prepared in Annealing buffer (10 mM Tris-HCl, pH 7.5, 50 mM NaCl) as follows: ssDNA and ssRNA were denatured at 95°C for 5 min to remove secondary structures and immediately snap-cooled on ice; dsDNA and dsRNA were generated by annealing equimolar 5'-FAM-labeled sense strands and unlabeled antisense strands at 95°C for 5 min, followed by gradual cooling to room temperature at 1°C/min; the tRNA substrate was folded by heating at 80°C for 5 min, cooling slowly to room temperature, and incubating at 37°C for 30 min to adopt native secondary structures.

The sequences of all synthetic oligonucleotides used in this study were as follows:

55-nt ssDNA and dsDNA substrates

Sense strand:

5'-FAM-AGCTGACGTTTGTACTCCAGCGTCTCATCTTTATGCGTCAGCAGAGATTTCTGCT-3'

Antisense strand:

5'-AGCAGAAATCTCTGCTGACGCATAAAGATGAGACGCTGGAGTACAAACGTCAGCT-3'

55-nt ssRNA and dsRNA substrates:

Sense strand:

5'-FAM-AGCUGACGUUUGUACUCCAGCGUCUCAUCUUUAUGCGUCAGCAGAGAUUUCUGCU-3'

Antisense strand:

5'-AGCAGAAAUCUCUGCUGACGCAUAAAGAUGAGACGCUGGAGUACAAACGUCAGCU-3'

Synthetic tRNA substrate:

5'-FAM-GCCGAAAUAGCUCAGUUGGGAGAGCGUUAGACAGAAGAUCUAAAGGUCCCUGGUU CGAUCCCGGGUUUCGGCACCA-3'.

663

664 **ATPase activity assay**

665 The ATPase activity of SAMD9C was quantified using the Malachite Green Phosphate Detection Kit
666 (Beyotime) following the manufacturer's protocol. Assays were conducted to evaluate the intrinsic
667 activity of SAMD9C alongside its truncation variants, as well as the allosteric modulation of
668 SAMD9C by nucleic acids or ε-NAD^+. Reaction mixtures (20 μl) were assembled in ATPase buffer
669 (20 mM HEPES, pH 7.5, 150 mM NaCl, 5 mM $MgCl_2$, 1 mM DTT) using 1 μM purified SAMD9C or
670 its designated truncation variants. To test potential allosteric effects, specified nucleic acid species
671 (including ssDNA, dsDNA, ssRNA, dsRNA, and tRNA at a final concentration of 2.5 μM) or ε-NAD+
672 (final concentration of 2.5 mM) were pre-incubated with SAMD9C at room temperature for 10 min.
673 Reactions were subsequently initiated by the addition of 1 mM ATP. After incubation at 37°C for 30
674 min in 96-well plates, the enzymatic reactions were quenched by adding EDTA to a final
675 concentration of 100 mM. Aliquots of the quenched mixtures were transferred and reacted with the
676 malachite green reagent for colorimetric development for 30 min at room temperature. The
677 absorbance at 630 nm was measured using an Envision Multimode Microplate Reader
678 (PerkinElmer). Phosphate concentrations were determined relative to a standard curve generated
679 concurrently. All experiments were performed in at least three independent replicates.

680

681 **NADase activity assay**

682 The NAD^+ hydrolysis activity of SAMD9C and its truncation variants was determined by quantifying
683 the production of ε-ADPR. Enzymatic cleavage of the nicotinamide glycosidic bond in ε-NAD^+ yields
684 ε-ADPR, which emits a distinct fluorescent signal. Assays were performed to compare SAMD9C
685 with its truncation variants under baseline conditions, and to assess the allosteric modulation of
686 SAMD9C by nucleic acids or ATP. Purified protein samples (1 μM) were prepared in reaction buffer
687 (20 mM HEPES, pH 7.5, 150 mM NaCl, 5 mM $MgCl_2$, 1 mM DTT). To evaluate potential allosteric
688 effects on SAMD9C, specified nucleic acid species (including ssDNA, dsDNA, ssRNA, dsRNA, and
689 tRNA at a final concentration of 2.5 μM) or ATP (final concentration of 2.5 mM) were pre-incubated
690 with SAMD9C at room temperature for 10 min prior to substrate addition. Reactions were initiated
691 by the addition of 50 μM ε-NAD^+. The mixtures were immediately transferred to an Envision
692 Multimode Microplate Reader (PerkinElmer), and fluorescence intensities were monitored
693 kinetically at 37°C every 2 min for 20 min, employing excitation and emission wavelengths of 310

nm and 410 nm, respectively. Initial velocity data were analyzed and plotted using GraphPad Prism. All experiments were performed in at least three independent replicates.

Data Availability

The cryo-EM density maps and corresponding atomic coordinates generated in this study have been deposited in the Electron Microscopy Data Bank (EMDB) and the Protein Data Bank (PDB), respectively, under the following accession codes:

Human SAMD9C monomer: EMD-82773 and PDB 44OU

C_2-symmetric dimer 1: EMD-81029 and PDB 27BE

C_2-symmetric dimer 2: EMD-81030 and PDB 27BF

C_2-symmetric dimer with an asymmetric OB domain: EMD-81031 and PDB 27BG

Asymmetric dimer 1: EMD-81032 and PDB 27BH

Asymmetric dimer 2: EMD-81033 and PDB 27BI

Asymmetric intermediate trimer: EMD-81034 and PDB 27BJ

ΔOB monomer: EMD-81045 and PDB 27BZ

ΔOB C_2-symmetric dimer: EMD-81046 and PDB 27CA

ΔOB asymmetric dimer: EMD-81047 and PDB 27CB

Source data are provided with this paper. All other data supporting the findings of this study are available from the corresponding author upon reasonable request.

Author Contributions

J.M. conceived and initiated the project, designed the study, and wrote the manuscript. X.Y. and Y.W. contributed to project design, supervised the study, and critically revised the manuscript. J.Z. performed protein expression and purification, biochemical assays, cryo-EM sample preparation, and data collection. X.C. assisted with protein production and biochemical analyses. H.W. contributed to protein expression and cryo-EM data processing. Z.L. performed the cryo-EM data processing and model building. K.Y. contributed to data analysis and manuscript revision. All authors discussed the results, reviewed, and approved the final manuscript.

Competing interests

The authors declare no competing interests.

Acknowledgements

Cryo-EM data collection was performed at the Structural Biology Core Facility of Shenzhen Medical Academy of Research and Translation (SMART) and the Center for Biological Imaging (CBI), Core Facilities for Protein Science, Institute of Biophysics (IBP), Chinese Academy of Sciences (CAS). We thank Boling Zhu and Xujing Li for their assistance with cryo-EM data collection, and Dr. Gang Fu at SMART for his assistance with TEM maintenance, cryo-EM sample screening, and data collection. We thank the Sample Preparation and Analysis Core Facility of the Bio-Tech Center of SMART for technical support with SPR and BLI analyses. This work was supported by grants from the Shenzhen Medical Research Fund (E24010010 and E24010013) and the Shenzhen Bay Laboratory Startup Fund (21330061) to J.M.

References

1 Lee, H. *et al.* Diverse bacterial pattern recognition receptors sense the core phage proteome. *Nature* (2026). https://doi.org/10.1038/s41586-026-10852-6

2 Leipe, D. D., Koonin, E. V. & Aravind, L. STAND, a class of P-loop NTPases including animal and plant regulators of programmed cell death: multiple, complex domain architectures, unusual phyletic patterns, and evolution by horizontal gene transfer. *Journal of molecular biology* **343**, 1–28 (2004).

3 Koonin, E. & Aravind, L. Origin and evolution of eukaryotic apoptosis: the bacterial connection. *Cell Death & Differentiation* **9**, 394–404 (2002).

4 Gao, L. *et al.* Diverse enzymatic activities mediate antiviral immunity in prokaryotes. *Science* **369**, 1077–1084 (2020).

5 Riedl, S. J., Li, W., Chao, Y., Schwarzenbacher, R. & Shi, Y. Structure of the apoptotic protease-activating factor 1 bound to ADP. *Nature* **434**, 926–933 (2005).

6 Zhou, M. *et al.* Atomic structure of the apoptosome: mechanism of cytochrome c-and dATP-mediated activation of Apaf-1. *Genes & development* **29**, 2349–2361 (2015).

7 Hu, Z. *et al.* Crystal structure of NLRC4 reveals its autoinhibition mechanism. *Science* **341**, 172–175 (2013).

8 Zhang, L. *et al.* Cryo-EM structure of the activated NAIP2-NLRC4 inflammasome reveals nucleated polymerization. *Science* **350**, 404–409 (2015).

9 Hu, Z. *et al.* Structural and biochemical basis for induced self-propagation of NLRC4. *Science* **350**, 399–404 (2015).

10 Wang, J. *et al.* (2019).

11 Wang, J. *et al.* Ligand-triggered allosteric ADP release primes a plant NLR complex. *Science* **364**, eaav5868 (2019).

12 Gao, L. A. *et al.* Prokaryotic innate immunity through pattern recognition of conserved viral proteins. *Science* **377**, eabm4096 (2022).

13 Mekhedov, S. L., Makarova, K. S. & Koonin, E. V. The complex domain architecture of SAMD9 family proteins, predicted STAND-like NTPases, suggests new links to inflammation and apoptosis. *Biology direct* **12**, 13 (2017).

14 Lemos de Matos, A., Liu, J., McFadden, G. & Esteves, P. J. Evolution and divergence of the mammalian SAMD9/SAMD9L gene family. *BMC evolutionary biology* **13**, 121 (2013).

15 Xiang, Y. Poxvirus host-range determinants: SAMD9/9L and beyond. *Annual review of virology* **12**, 93–114 (2025).

16 Liu, J. & McFadden, G. SAMD9 is an innate antiviral host factor with stress response properties that can be antagonized by poxviruses. *Journal of virology* **89**, 1925–1931 (2015).

17 Zhang, F. *et al.* Human SAMD9 is a poxvirus-activatable anticodon nuclease inhibiting codon-specific protein synthesis. *Science Advances* **9**, eadh8502 (2023).

18 Liu, J., Wennier, S., Zhang, L. & McFadden, G. M062 is a host range factor essential for myxoma virus pathogenesis and functions as an antagonist of host SAMD9 in human cells. *Journal of virology* **85**, 3270–3282 (2011).

19 Meng, X. *et al.* A paralogous pair of mammalian host restriction factors form a critical host barrier against poxvirus infection. *PLoS pathogens* **14**, e1006884 (2018).

20 Meng, X., Krumm, B., Li, Y., Deng, J. & Xiang, Y. Structural basis for antagonizing a host restriction factor by C7 family of poxvirus host-range proteins. *Proceedings of the National Academy of Sciences* **112**, 14858–14863 (2015).

21 Sivan, G., Ormanoglu, P., Buehler, E. C., Martin, S. E. & Moss, B. Identification of restriction factors by human genome-wide RNA interference screening of viral host range mutants exemplified by

discovery of SAMD9 and WDR6 as inhibitors of the vaccinia virus K1L− C7L− mutant. *MBio* **6**, 10.1128/mbio. 01122–01115 (2015).

22 Hou, G. *et al.* SAMD9 senses cytosolic double-stranded nucleic acids in epithelial and mesenchymal cells to induce antiviral immunity. *Nature communications* **16**, 3756 (2025).

23 Legrand, A. *et al.* Evolutionary characterization of antiviral SAMD9/9L across kingdoms supports ancient convergence and lineage-specific adaptations. *Nature Ecology & Evolution* **9**, 2206–2222 (2025).

24 Legrand, A. *et al.* SAMD9L acts as an antiviral factor against HIV-1 and primate lentiviruses by restricting viral and cellular translation. *PLoS biology* **22**, e3002696 (2024).

25 Cannac, M. *et al.* SAMD9L inhibits flavivirus translation independently of its capacity to trigger innate immune response. *PLoS Pathogens* **21**, e1013773 (2025).

26 Narumi, S. *et al.* SAMD9 mutations cause a novel multisystem disorder, MIRAGE syndrome, and are associated with loss of chromosome 7. *Nature genetics* **48**, 792–797 (2016).

27 Buonocore, F. *et al.* Somatic mutations and progressive monosomy modify SAMD9-related phenotypes in humans. *The Journal of clinical investigation* **127**, 1700–1713 (2017).

28 Chen, D.-H. *et al.* Ataxia-pancytopenia syndrome is caused by missense mutations in SAMD9L. *The American Journal of Human Genetics* **98**, 1146–1158 (2016).

29 Tesi, B. *et al.* Gain-of-function SAMD9L mutations cause a syndrome of cytopenia, immunodeficiency, MDS, and neurological symptoms. *Blood, The Journal of the American Society of Hematology* **129**, 2266–2279 (2017).

30 Schwartz, J. R. *et al.* The genomic landscape of pediatric myelodysplastic syndromes. *Nature communications* **8**, 1557 (2017).

31 Wong, J. C. *et al.* Germline SAMD9 and SAMD9L mutations are associated with extensive genetic evolution and diverse hematologic outcomes. *JCI insight* **3**, e121086 (2018).

32 Knight, M. J., Leettola, C., Gingery, M., Li, H. & Bowie, J. U. A human sterile alpha motif domain polymerizome. *Protein Science* **20**, 1697–1706 (2011).

33 Peng, S. *et al.* Structure and function of an effector domain in antiviral factors and tumor suppressors SAMD9 and SAMD9L. *Proceedings of the National Academy of Sciences* **119**, e2116550119 (2022).

34 Holm, L. Dali server: structural unification of protein families. *Nucleic acids research* **50**, W210–W215 (2022).

35 Zhao, K., Chai, X. & Marmorstein, R. Structure of the yeast Hst2 protein deacetylase in ternary complex with 2′-O-acetyl ADP ribose and histone peptide. *Structure* **11**, 1403–1411 (2003).

36 Alfieri, C., Chang, L. & Barford, D. Mechanism for remodelling of the cell cycle checkpoint protein MAD2 by the ATPase TRIP13. *Nature* **559**, 274–278 (2018).

37 Roy, M. J. *et al.* Structural mapping of PEAK pseudokinase interactions identifies 14-3-3 as a molecular switch for PEAK3 signaling. *Nature communications* **14**, 3542 (2023).

38 Yang, X.-J. *et al.* Crystal structure of a Y-box binding protein 1 (YB-1)–RNA complex reveals key features and residues interacting with RNA. *Journal of Biological Chemistry* **294**, 10998–11010 (2019).

39 Bravo, J. P., Ramos, D. A., Fregoso Ocampo, R., Ingram, C. & Taylor, D. W. Plasmid targeting and destruction by the DdmDE bacterial defence system. *Nature* **630**, 961–967 (2024).

40 Loeff, L. *et al.* Molecular mechanism of plasmid elimination by the DdmDE defense system. *Science* **385**, 188–194 (2024).

41 Wang, Y., Tian, Y., Yang, X., Yu, F. & Zheng, J. Filamentation activates bacterial Avs5 antiviral protein. *Nature Communications* **16**, 2408 (2025).

42 Muralidharan, A. *et al.* Molecular basis for anti-jumbo phage immunity by AVAST Type 5. *Molecular Cell* **86**, 740–756. e749 (2026).

43 Maekawa, S., Ohto, U., Shibata, T., Miyake, K. & Shimizu, T. Crystal structure of NOD2 and its implications in human disease. *Nature communications* **7**, 11813 (2016).

44 Sahoo, S. S. *et al.* Clinical evolution, genetic landscape and trajectories of clonal hematopoiesis in SAMD9/SAMD9L syndromes. *Nature medicine* **27**, 1806–1817 (2021).

45 Sahoo, S. S., Erlacher, M. & Wlodarski, M. W. Genetic and clinical spectrum of SAMD9 and SAMD9L syndromes: from variant interpretation to patient management. *Blood* **145**, 475–485 (2025).

46 Sharif, H. *et al.* Structural mechanism for NEK7-licensed activation of NLRP3 inflammasome. *Nature* **570**, 338–343 (2019).

47 Hochheiser, I. V. *et al.* Structure of the NLRP3 decamer bound to the cytokine release inhibitor CRID3. *Nature* **604**, 184–189 (2022).

48 Xiao, L., Magupalli, V. G. & Wu, H. Cryo-EM structures of the active NLRP3 inflammasome disc. *Nature* **613**, 595–600 (2023).

49 Kim, C. A., Gingery, M., Pilpa, R. M. & Bowie, J. U. The SAM domain of polyhomeotic forms a helical polymer. *Nature structural biology* **9**, 453–457 (2002).

50 Baron, M. K. *et al.* An architectural framework that may lie at the core of the postsynaptic density. *Science* **311**, 531–535 (2006).

51 Thanos, C. D., Goodwill, K. E. & Bowie, J. U. Oligomeric structure of the human EphB2 receptor SAM domain. *Science* **283**, 833–836 (1999).

52 Mastronarde, D. N. Automated electron microscope tomography using robust prediction of specimen movements. *Journal of structural biology* **152**, 36–51 (2005).

53 Punjani, A., Rubinstein, J. L., Fleet, D. J. & Brubaker, M. A. cryoSPARC: algorithms for rapid unsupervised cryo-EM structure determination. *Nat Methods* **14**, 290–296 (2017). https://doi.org/10.1038/nmeth.4169

54 Bepler, T. *et al.* Positive-unlabeled convolutional neural networks for particle picking in cryo-electron micrographs. *Nature methods* **16**, 1153–1160 (2019).

55 Abramson, J. *et al.* Accurate structure prediction of biomolecular interactions with AlphaFold 3. *Nature* **630**, 493–500 (2024). https://doi.org/10.1038/s41586-024-07487-w

56 Pettersen, E. F. *et al.* UCSF ChimeraX: Structure visualization for researchers, educators, and developers. *Protein Sci* **30**, 70–82 (2021). https://doi.org/10.1002/pro.3943

57 Casanal, A., Lohkamp, B. & Emsley, P. Current developments in Coot for macromolecular model building of Electron Cryo-microscopy and Crystallographic Data. *Protein Sci* **29**, 1069–1078 (2020). https://doi.org/10.1002/pro.3791

58 Afonine, P. V. *et al.* Real-space refinement in PHENIX for cryo-EM and crystallography. *Acta Crystallogr D Struct Biol* **74**, 531–544 (2018). https://doi.org/10.1107/S2059798318006551

59 Williams, C. J. *et al.* MolProbity: more and better reference data for improved all‐atom structure validation. *Protein science* **27**, 293–315 (2018).

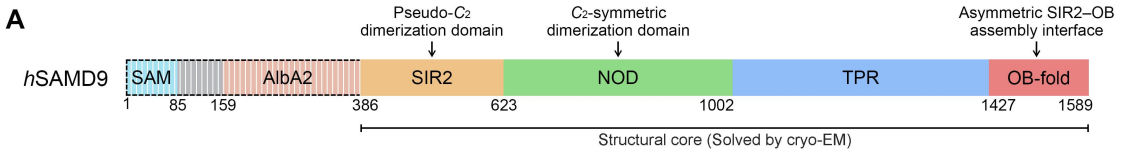

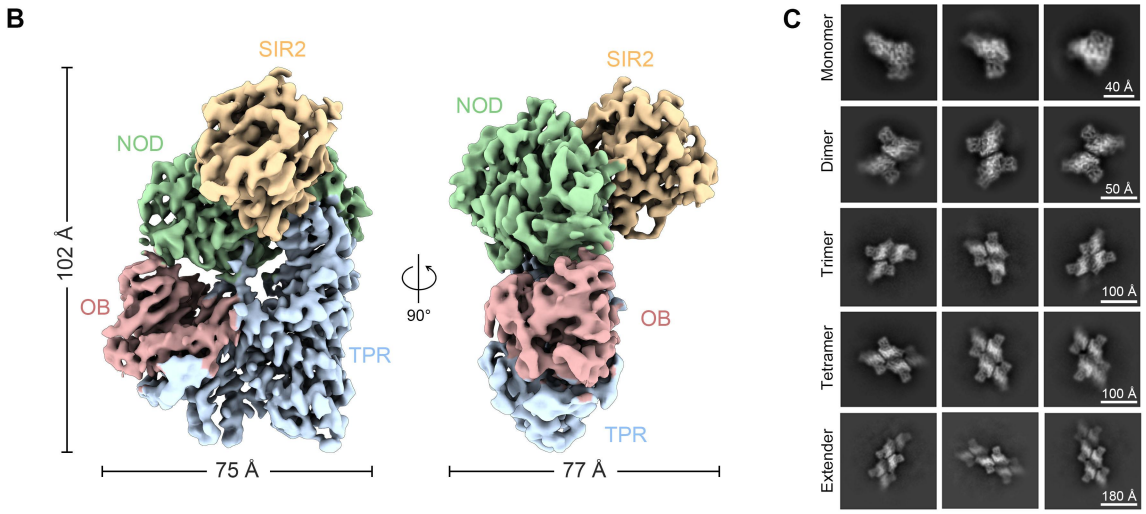

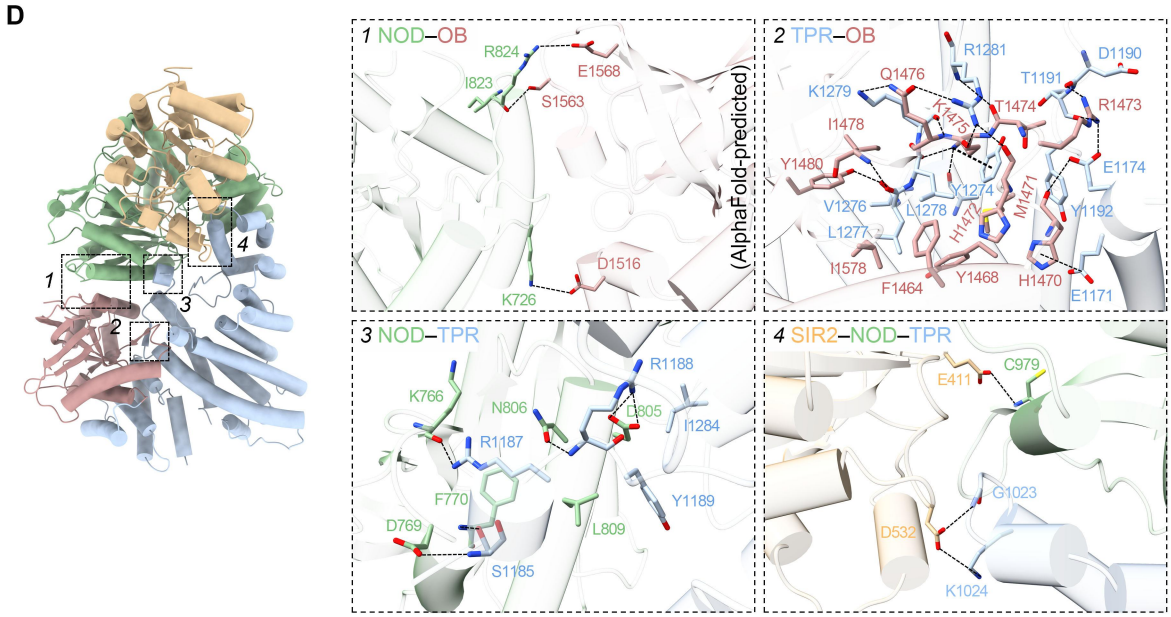

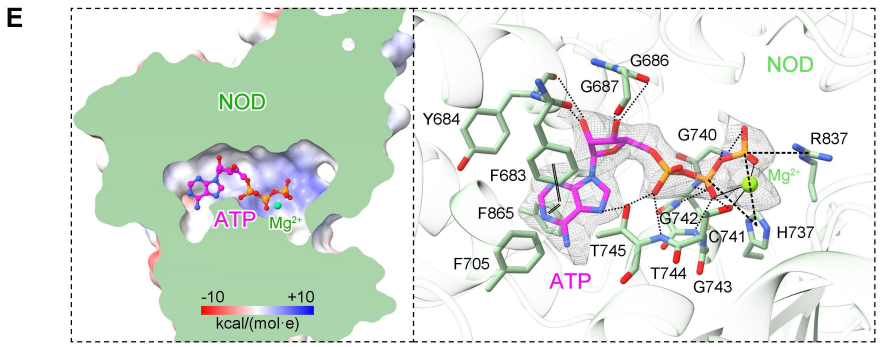

Figure 1. Overall architecture of the SAMD9 monomer resolved by cryo-EM

(**A**) Domain organization of human SAMD9. Domains are color-coded as follows: SAM (light blue hatched bar), AlbA2 (light pink hatched bar), SIR2 (wheat), NOD (dark green), TPR (blue), and OB fold (salmon). Residue boundaries, resolved regions by cryo-EM (solid bars), unresolved regions (hatched bars), and key inter-domain interactions (arrows/connecting lines) are indicated.

(B) Two orthogonal views of the cryo-EM map of the compact SAMD9 monomer, displaying a G-shaped, closed conformation with approximate dimensions. The map is segmented and color-coded by domain as in panel **A**.

(**C**) Representative 2D class averages showing the oligomeric equilibrium of SAMD9, including monomers (~40%), dimers (~30%), trimers (~10%), tetramers (~15%), and extended filaments (~5%). Scale bars are shown for each class.

(**D**) Cartoon representation of the SAMD9 monomer highlighting intramolecular interactions that lock the closed autoinhibited conformation (four dashed boxes, left), with close-up views (right): (1) NOD–OB (AlphaFold-predicted); (2) TPR–OB; (3) NOD–TPR; (4) tripartite SIR2–NOD–TPR. Interacting side chains are shown as sticks; hydrogen bonds/salt bridges as dashed lines; the cation–π interaction (K1475–Y1274) is marked by a thick dashed line.

(**E**) Endogenously bound ATP (magenta sticks) within the NOD catalytic pocket. Left: Electrostatic surface potential. Right: Cryo-EM map (transparent mesh) showing ATP co-coordinated by a Mg^{2+} ion (green sphere) and P-loop residues (Y684, F683, F865, G686, G687, G740–T745, H737, R837).

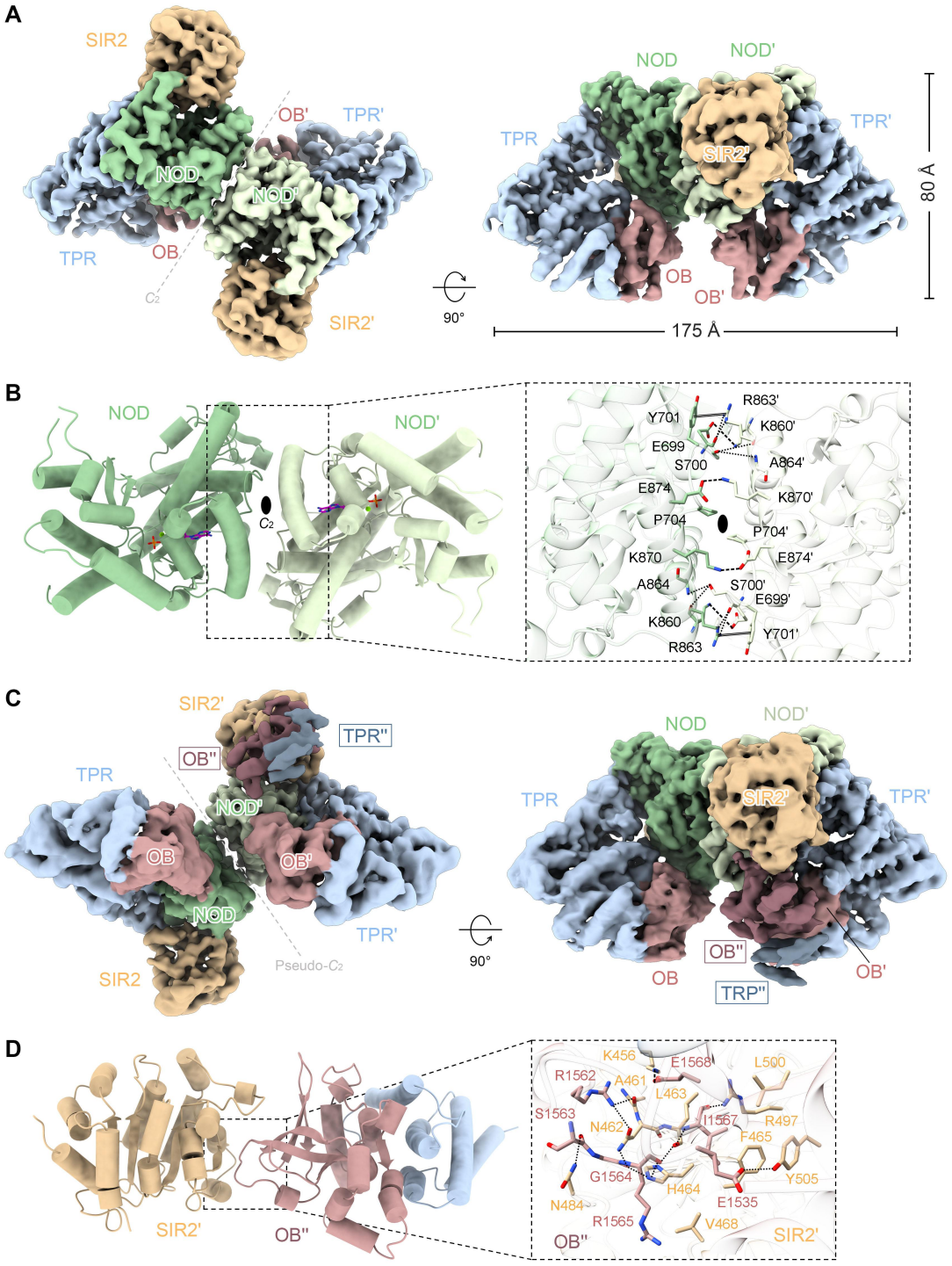

Figure 2. Structural basis of C_2-symmetric SAMD9 dimerization and asymmetric assembly

(A) Two orthogonal views of the cryo-EM map of the C_2-symmetric SAMD9 dimer with approximate dimensions. Protomers are segmented and color-coded by domain as defined in Figure 1 (Protomer 1: SIR2, NOD, TPR, OB; Protomer 2: SIR2', NOD', TPR', OB'). For clarity, NOD' is colored light green to distinguish it from NOD. The C_2 symmetry axis is indicated by a dashed line.

(B) Structural basis of C_2-symmetric dimerization mediated by the NOD–NOD' interface, showing an overall view of the interface (left) and a close-up view of the interacting residue network (right) anchored along the twofold symmetry axis (C_2).

(**C**) Two orthogonal views of the cryo-EM map of an asymmetric partial trimer assembly, featuring additional density for OB'' and TPR'' domains bound to the dimeric core.

(**D**) Structural basis of the asymmetric interaction mediated by the SIR2'–OB'' interface, showing an overview of the interface (left) and a close-up view of the interacting residue network (right). In panels **B** and **D**, proteins are depicted in cartoon representation; interacting side chains are shown as sticks; hydrogen bonds and salt bridges are indicated by dashed lines; the cation–π interaction is marked by a thick dashed line.

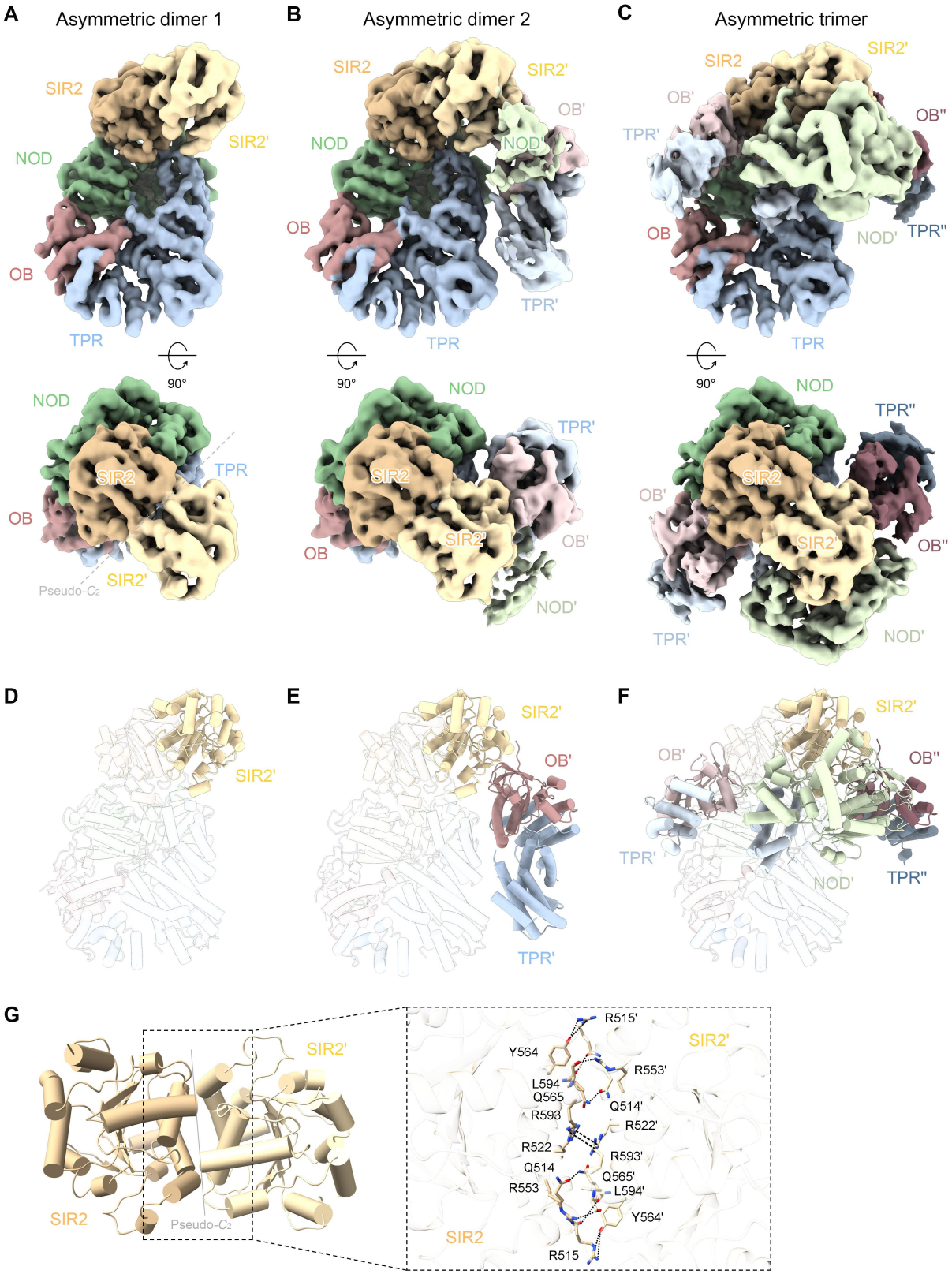

Figure 3. Conformational heterogeneity of asymmetric SAMD9 assemblies

(A–C) Two orthogonal views of cryo-EM density maps representing distinct asymmetric oligomeric species captured during 3D classification: (**A**) Asymmetric dimer 1, in which a sole SIR2' domain mediates pseudo-C_2 association primarily via a SIR2–SIR2' interface. (**B**) Asymmetric dimer 2, in which the second protomer (partially solved) adopts an "open" conformation; asymmetric packing is mediated by the same SIR2–SIR2' interface as in asymmetric dimer 1, with its partial TPR'–OB' module interacting directly with the SIR2' domain. (**C**) Asymmetric trimer 2, in which the second protomer, comprising a complete SIR2'-NOD' module and a partial TPR'–OB' module, engages protomer 1 via the SIR2–SIR2' interface, with its partial TPR'–OB' module binding to the SIR2 domain of protomer 1. The third protomer consists of solely a partial TPR''–OB'' module that interacts with protomer 2 in a manner analogous to the TPR'–OB' module in asymmetric dimer 2.

(**D–F**) Corresponding structural models for asymmetric dimer 1 (**D**), asymmetric dimer 2 (**E**), and asymmetric trimer 2 (**F**), illustrating the conformational heterogeneity and large-scale spatial reorganization of the peripheral SIR2', TPR'–OB', and TPR''–OB'' modules relative to the rigid, closed protomer 1. All three asymmetric assemblies are shown in matching orientations for direct comparison; the identical, compactly closed protomer 1 is depicted as a semi-transparent cartoon, whereas the other protomers/modules are segmented and color-coded by domain as defined in Figure 1.

(**G**) Structural basis of pseudo-C_2-symmetric dimerization mediated by the SIR2–SIR2' interface, shared by asymmetric dimers 1 and 2 and asymmetric trimer 2. Shown are an overall view of the interface (left) and a close-up view of the interacting residue network (right) centered on the pseudo-twofold symmetry axis (pseudo-C_2). Proteins are shown in cartoon representation; interacting side chains are displayed as sticks; hydrogen bonds and salt bridges are indicated by dashed lines.

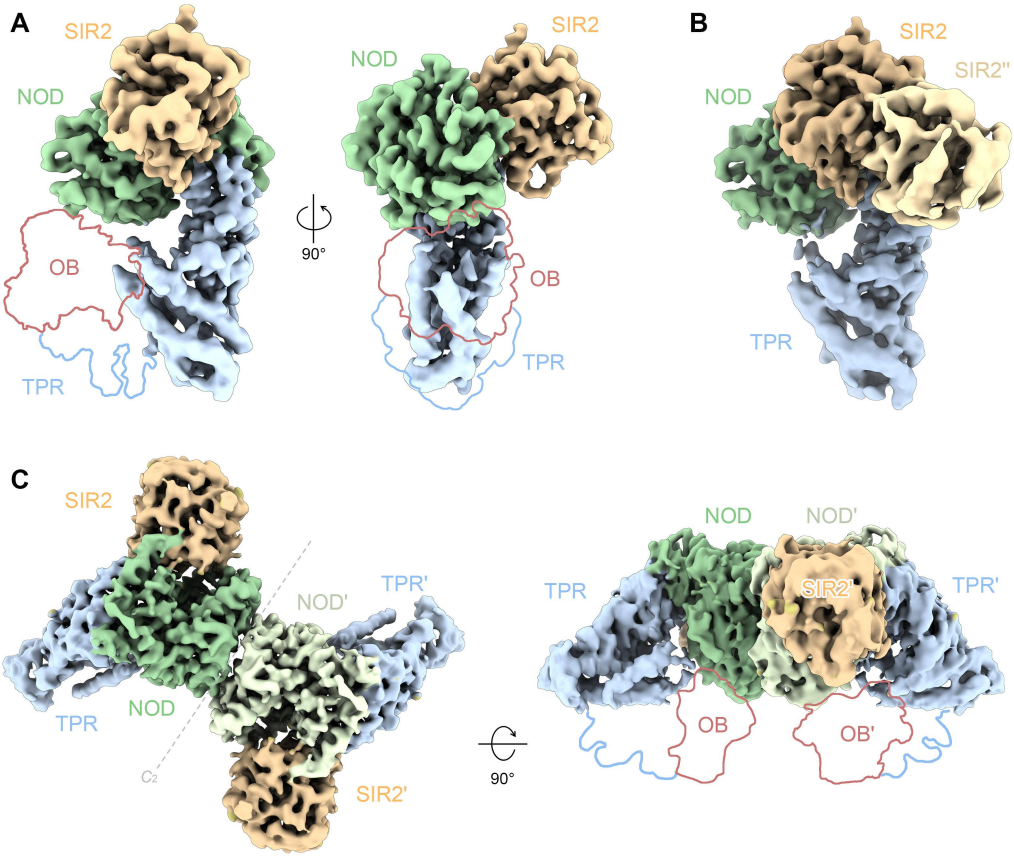

Figure 4. Cryo-EM structures of the AlbA2 and OB domain-truncated SAMD9 variant (SAMD9$^{\Delta AlbA2\Delta OB}$)
(**A**) Two orthogonal views of the cryo-EM density map of monomeric SAMD9$^{\Delta AlbA2\Delta OB}$. Density is segmented and colored by domain as in Figure 1. Red outline denotes the truncated OB domain; blue outline indicates the disordered C-terminal region of the TPR domain relative to the wild-type monomer.
(**B**) Density map of a partially asymmetric dimer, comprising a SAMD9$^{\Delta AlbA2\Delta OB}$ monomer bound to an additional SIR2 domain (SIR2'', light yellow). The orientation matches panel **A** (left) for direct comparison.
(**C**) Two orthogonal views of the C_2-symmetric SAMD9$^{\Delta AlbA2\Delta OB}$ dimer, with the symmetry axis shown as a dashed line. Protomers are distinguished by prime (') symbols, with NOD and NOD' colored dark green and light green, respectively. Red and blue outlines mark the truncated OB domains and disordered TPR C-terminal regions, respectively. The maintenance of the core dimeric scaffold despite OB truncation highlights the structural integrity of the SIR2–NOD–TPR module.

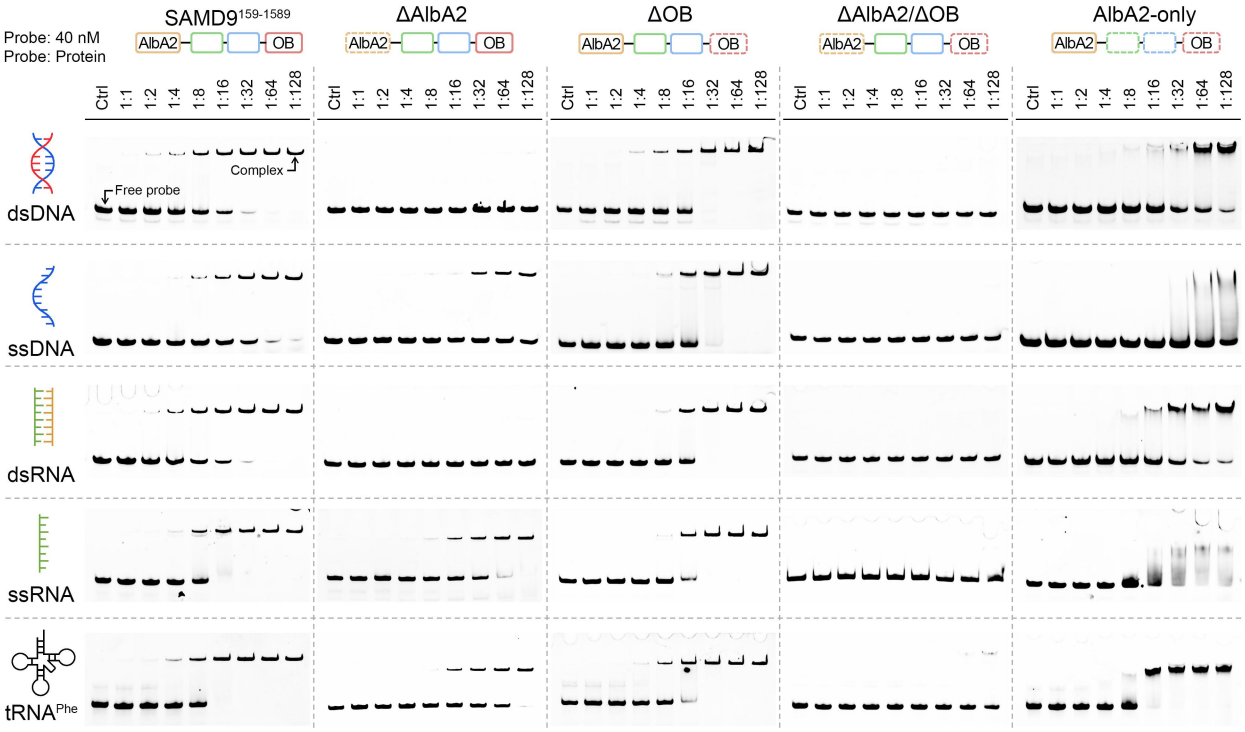

Figure 5. Comprehensive nucleic acid binding profiling of SAMD9C

Electrophoretic mobility shift assays (EMSAs) evaluating the binding capacities of wild-type (WT) SAMD9 (SAMD9$^{159–1589}$) and domain-deletion variants (ΔAlbA2, ΔOB, ΔAlbA2/ΔOB, and AlbA2-only) against a panel of FAM-labeled nucleic acid substrates (dsDNA, ssDNA, dsRNA, ssRNA, and tRNA^{Phe}; 40 nM). Each column represents a distinct SAMD9 construct, arranged from left to right as WT SAMD9$^{159–1589}$, ΔAlbA2, ΔOB, ΔAlbA2/ΔOB, and AlbA2-only. Construct schematics are shown at the top (solid boxes, retained domains; dashed outlines, deleted regions), with representative cartoons of nucleic acid substrates positioned on the left. Purified proteins were titrated at the indicated molar ratios (probe:protein, 1:1 to 1:128) and resolved on non-denaturing gels; protein-free lanes served as negative controls (Ctrl). Migration positions of free probes and protein–nucleic acid complexes are indicated by representative labels and arrows. WT SAMD9 exhibits the most extensive binding activity across all tested substrates. The isolated AlbA2 domain retains intrinsic binding activity toward diverse nucleic acids, whereas the OB domain preferentially contributes to single-stranded species, , including ssDNA, ssRNA, and tRNA. Constructs retaining the central modules (WT and ΔOB) display markedly enhanced binding relative to AlbA2 alone, whereas simultaneous deletion of both AlbA2 and OB domains (ΔAlbA2/ΔOB) abolishes nucleic acid engagement. Representative gels from three independent experiments are shown.

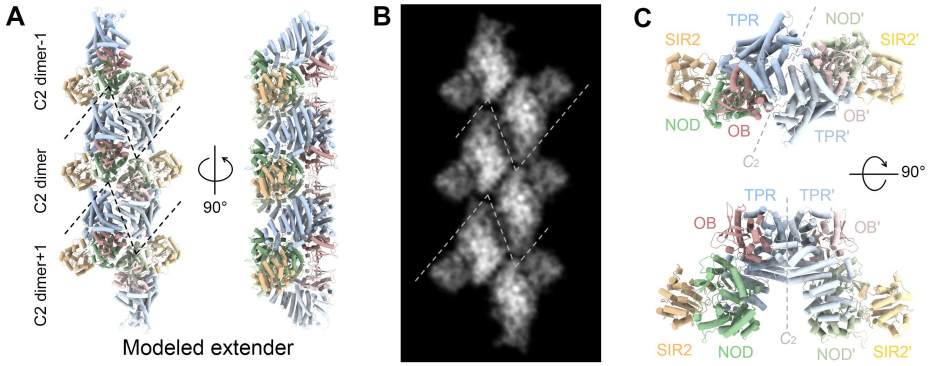

Figure 6. Structural model of the SAMD9C higher-order assembly

(**A**) Cartoon representation of the modeled SAMD9C assembly ("Modeled extender") formed by repeating C_2-symmetric dimeric units guided by 2D class average analysis, shown in two orthogonal views rotated by 90°. Dashed lines indicate the interfaces between adjacent C_2-symmetric dimeric units.

(**B**) Simulated low-resolution projection map of the modeled SAMD9C extender corresponding to the structural views in Panel **A**, as well as the experimental 2D class averages shown in Figure 1C. Dashed lines delineate the boundaries between adjacent C_2-symmetric dimeric units along the assembly interface.

(**C**) Detailed view of the alternative C_2 dimer formed between individual C_2-symmetric dimeric units that drives extender formation, shown in two orthogonal views (rotated by 90°). Equivalent structural domains for both protomers are labeled and color-coded according to the scheme used in Figure 1. The C_2 symmetry axis is indicated by dashed lines.

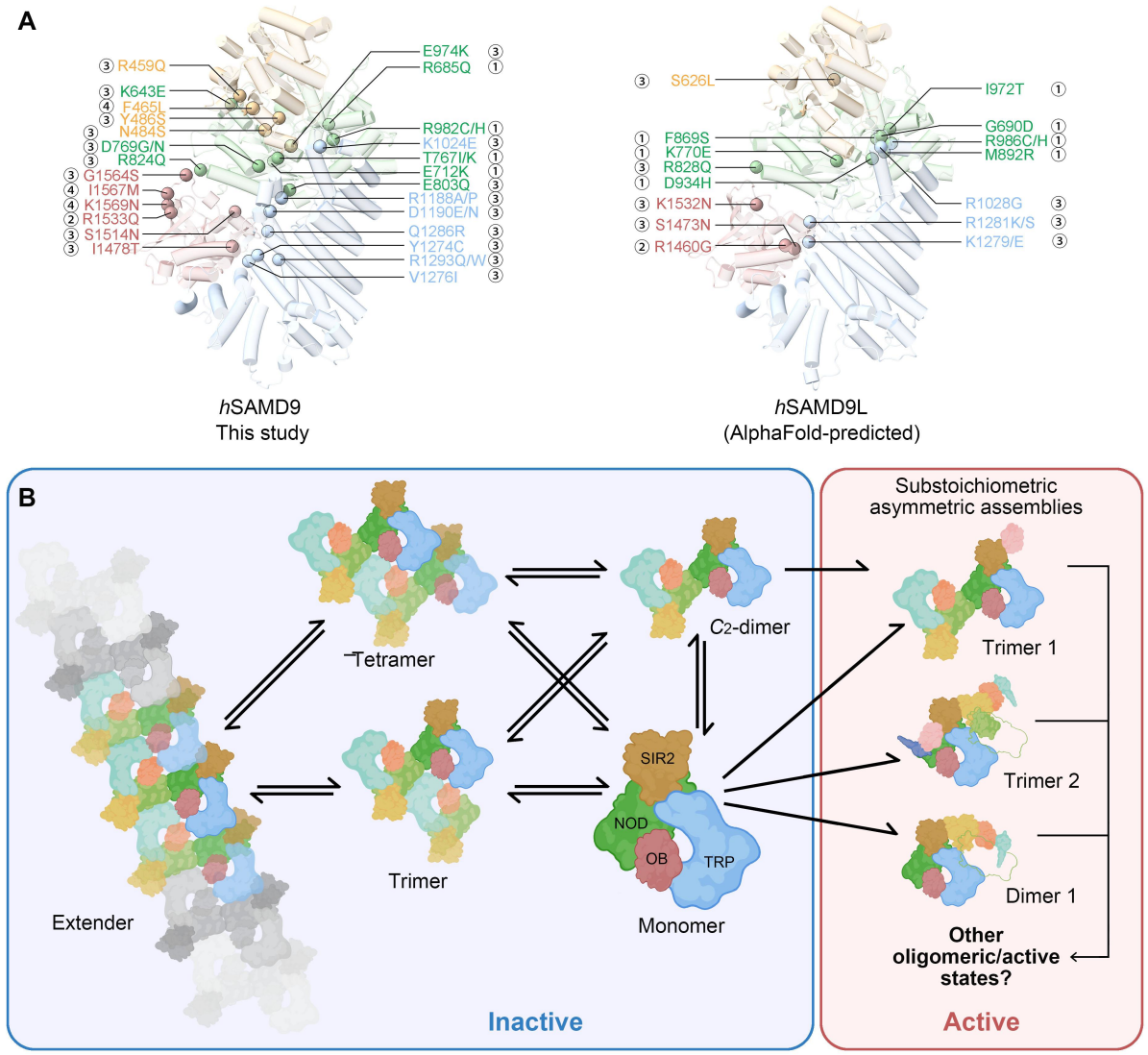

Figure 7. Structural mapping of pathogenic mutations and proposed regulatory model of SAMD9

(**A**) Mapping and classification of germline *SAMD9/SAMD9L* mutations linked to MIRAGE syndrome, hematologic malignancies, and autoinflammatory diseases onto human SAMD9 (left) and SAMD9L (right, AlphaFold model). Selected pathogenic variants (spheres) are categorized into four classes: Class 1, NOD conformational dynamics and ATP-binding sites; Class 2, OB-domain-mediated nucleic acid sensing; Class 3, intraprotomer autoinhibitory interfaces; and Class 4, asymmetric SIR2–OB assembly interfaces.

(**B**) Proposed mechanism for SAMD9 homeostasis and activation. **Resting State** (left): Basal SAMD9 adopts a compact, closed monomer that self-assembles via NOD–NOD interactions into C_2-symmetric dimers and higher-order supramolecular assemblies (tetramers/filaments), maintaining SAMD9 in a restrained state. **Alternative/Activated State** (right): Recognition of PAMPs (e.g., viral nucleic acids) via the OB domain may promote remodeling of these assemblies and favor asymmetric oligomeric states, involving inter-subunit SIR2–SIR2 and SIR2–OB interactions. Such rearrangements could relieve autoinhibitory interactions in at least one protomer and generate a partially open intermediate state. Whether SAMD9 forms higher-order ring-like effector assemblies analogous to inflammasomes or plant resistosomes remains to be determined. Disease-associated LoF and GoF variants may disrupt these regulatory checkpoints and shift the conformational and oligomeric equilibrium by either pathologically hyperactivating the protein or trapping it in a hyper-inhibited state to drive pathogenesis. Solid boxes indicate molecular component annotations; protomers are color-coded by domain as in Figure 1.